

FROM X-RAY DIPS TO ECLIPSE: WITNESSING DISK REFORMATION IN THE RECURRENT NOVA USCO

J.-U. NESS¹, B.E. SCHAEFER², A. DOBROTKA^{3,4}, A. SADOWSKI⁵, J.J. DRAKE⁶, R. BARNARD⁶, A. TALAVERA¹, R. GONZALEZ-RIESTRA¹, K.L. PAGE⁷, M. HERNANZ⁸, G. SALA⁹, S. STARRFIELD¹⁰

Draft version January 20, 2013

ABSTRACT

The 10th recorded outburst of the recurrent eclipsing nova U Sco was observed simultaneously in X-ray, UV, and optical by *XMM-Newton* on days 22.9 and 34.9 after outburst. Two full passages of the companion in front of the nova ejecta were observed, witnessing the reformation of the accretion disk.

On day 22.9, we observed smooth eclipses in UV and optical but deep dips in the X-ray light curve which disappeared by day 34.9, then yielding clean eclipses in all bands. X-ray dips can be caused by clumpy absorbing material that intersects the line of sight while moving along highly elliptical trajectories. Cold material from the companion could explain the absence of dips in UV and optical light. The disappearance of X-ray dips before day 34.9 implies significant progress in the formation of the disk.

The X-ray spectra contain photospheric continuum emission plus strong emission lines, but no clear absorption lines. Both continuum and emission lines in the X-ray spectra indicate a temperature increase from day 22.9 to day 34.9. We find clear evidence in the spectra and light curves for Thompson scattering of the photospheric emission from the white dwarf. Photospheric absorption lines can be smeared out during scattering in a plasma of fast electrons. We also find spectral signatures of resonant line scattering that lead to the observation of the strong emission lines. Their dominance could be a general phenomenon in high-inclination systems such as Cal 87.

Subject headings: novae, cataclysmic variables - stars: individual (U Sco)

1. INTRODUCTION

A nova outburst is a thermonuclear explosion on the surface of a white dwarf star. The energy is produced by fusion of hydrogen to helium and is released via complex radiation transport processes through the optically thick ejecta, spanning a broad wavelength range. As the density of the ejecta decreases with time, the peak of the radiation output continuously shifts from long wavelength optical emission to shorter wavelengths. The decreasing density allows us to see deeper into the outflow where the temperature and thus the energy of the emitted radiation is higher. Nova explosions occur in binary systems because the required amount of hydrogen-rich burning material can only be obtained by accretion from a sec-

ond star that orbits the white dwarf at a close enough distance to allow mass transfer via an accretion disk, see e.g., Robinson (1976). Once all the previously accreted hydrogen is consumed, the nova will turn off, gradually returning to the original condition of the system. A nova outburst does not significantly change the system parameters, and mass transfer can set in again, leading to new accumulation of hydrogen-rich material. Typically, the accumulation of sufficient hydrogen for another outburst is expected to take $\sim 10^4 - 10^5$ years, except for a handful of recurrent novae, in which this cycle occurs fast enough that more than one outburst has been observed in a human lifetime (Schaefer 2010).

During the initial blast, the accretion disk is destroyed, which was recently shown for U Sco by Drake & Orlando (2010) utilizing hydrodynamic models. One question of interest is how quickly it reforms. This is not well known, and opportunities of direct observations of the reformation process are rare. Significant theoretical efforts have been undertaken to understand the formation of accretion disks. An illustration of the expected formation process via Roche Lobe overflow is shown in fig. 1 in a review paper by Verbunt (1982). Initially, the gas streams with supersonic velocity along a highly eccentric orbit. As the stream hits the incoming gases, the flow downstream changes into a circular orbit, which is expected to occur on time scales longer than radiative cooling and the dynamical or orbital timescale. In most cases, viscosity plays an important role for the details, but this fundamental picture remains the same. More important should be the presence of intensive high-energy radiation during the times of the *XMM-Newton* observations of U Sco. The recurrent outbursts in the eclipsing sys-

¹ XMM-Newton Science Operations Centre, ESA, PO Box 78, 28691 Villanueva de la Cañada, Madrid, Spain, juness@sciops.esa.int

² Department of Physics and Astronomy, Louisiana State University, Baton Rouge, Louisiana, 70803, USA

³ Department of Physics, Institute of Materials Science, Faculty of Materials Science and Technology, Slovak University of Technology, Jána Bottu 25, 91724 Trnava, The Slovak Republic

⁴ Department of Astronomy, Graduate School of Science, Kyoto University, Sakyo-ku, Kyoto 606-8502, Japan

⁵ N. Copernicus Astronomical Center, Polish Academy of Sciences, Bartycka 18, 00-716 Warszawa, Poland

⁶ Harvard-Smithsonian Center for Astrophysics, 60 Garden Street, Cambridge, MA 02138, USA

⁷ Department of Physics & Astronomy, University of Leicester, Leicester, LE1 7RH, UK

⁸ Institut de Ciències de l'Espai (CSIC-IEEC), Campus UAB, Facultat de Ciències, C5 parell 2^{on}, 08193 Bellaterra (Barcelona), Spain

⁹ Departament Física i Enginyeria Nuclear, EUETIB (UPC-IEEC), Comte d'Urgell 187, 08036 Barcelona, Spain

¹⁰ School of Earth and Space Exploration, Arizona State University, Tempe, AZ 85287-1404, USA

tem U Sco are a unique laboratory to observe the earliest stages of the disk formation.

U Sco is a recurrent nova with now 10 recorded outbursts since 1863. The latest outburst was discovered by B. Harris on 2010 Jan 28.4385 (=HJD 2455224.94346) at $V = 7.8$ mag (Schaefer et al. 2010a). Schaefer et al. (2010b) extrapolated the light curve to earlier times, indicating that the peak magnitude was $V = 7.5$ on 2010 Jan 28.1 (=JD 2455224.605), and that the time of outburst was

$$t_0 = 2010\text{Jan}27.8 \text{ (= JD 2455224.305)}. \quad (1)$$

This time is used as the reference time t_0 in this article. The underlying system was identified as an eclipsing system by Schaefer (1990) with an inclination angle of $\gtrsim 80^\circ$ (Thoroughgood et al. 2001). Based on 29 accurate eclipse times from 2001-2009, we find a best fit linear ephemeris in units of days to be

$$HJD_{\min} = 2451234.5387 + E * 1.23054695, \quad (2)$$

where E is an integer that counts the cycles. The binary separation is $6.5 \pm 0.4 R_\odot$ (Schaefer 1990), and the component masses have been determined by Thoroughgood et al. (2001) to be $> 1.31 M_\odot$ for the white dwarf and $0.88 \pm 0.17 M_\odot$ for the secondary. The radius of the companion is $2.1 \pm 0.2 R_\odot$, indicating that it is evolved (Schaefer 1990). The high mass of the white dwarf, close to the Chandrasekhar mass limit, is consistent with the short recurrence time scale and led to speculations that U Sco may be a supernova Ia progenitor (Starrfield et al. 1988). However, recent abundance measurements by Mason (2011) indicate that the underlying white dwarf may of the ONeMg kind which does not contain enough nuclear binding energy for a SN Ia explosion. Consequently, even if the Chandrasekhar mass limit is reached, the white dwarf may turn into a neutron star via core collapse.

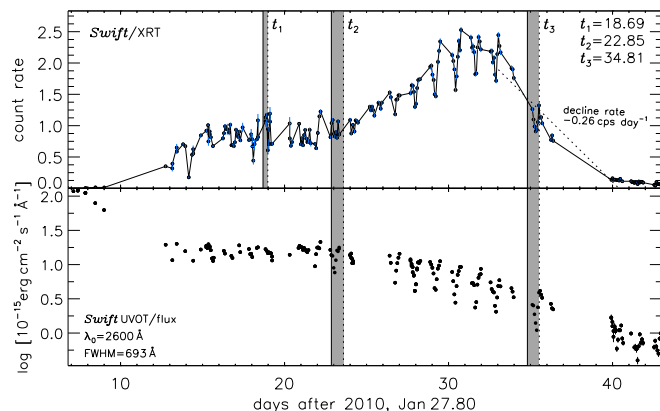


FIG. 1.— *Swift*/XRT (top) and UVOT (bottom) light curves of U Sco. The shaded regions mark the duration of continuous, deeper *Chandra* (t_1) and *XMM-Newton* (t_2 and t_3) observations.

Swift X-ray and UV monitoring started within a day after discovery (Schlegel et al. 2010a, but there was no X-ray detection until 2010 Jan 31 (day 4). The *Swift* X-ray and UV light curves shown in Fig. 1 will be discussed in more detail by Pagnotta et al. (in preparation). Until \sim day 8, the X-ray light curve was essentially constant with weak, hard emission above 3 keV (Schlegel et al.

2010a). On \sim day 12, the *Swift* count rate was found to be 100 times higher, exhibiting a supersoft spectrum (Schlegel et al. 2010b) that resembles the class of supersoft sources (SSS, Kahabka & van den Heuvel 1997; van den Heuvel et al. 1992). At the same time, until \sim day 12, the UV flux dramatically decreased, supporting the picture of a shrinking photospheric radius, accompanied by a continuous increase in photospheric temperature. Between days 12 and 25, no changes in X-ray and UV brightness were seen, while after day 25, another increase in X-rays with a simultaneous decrease in UV emission level occurred. From day 14.25 - 17.54 after discovery, two well covered, and one partly covered, eclipses were seen in the UV light curve by Osborne et al. (2010) who also reported that, in X-rays, no clear, sharp, deep or total eclipses were seen. The X-ray light curve was highly variable with typically lower flux around the time of eclipse. Around 2010 Mar 8 (day $t_0 + \sim 40$ days), the brightness of U Sco experienced a sharp drop in the X-ray/UV/Optical/IR bands (Schaefer et al. 2010c), indicating that nuclear burning had turned off.

Reports of deeper and continuous *Chandra* and *XMM-Newton* observations taken on 2010 February 14 and 19 ($t_1 = t_0 + 18.7$ and $t_2 = t_0 + 22.9$ days), respectively were given by Orio et al. (2010) and Ness et al. (2010). The times of these observations plus a second *XMM-Newton* observation taken on $t_3 = t_0 + 34.9$ days are marked by gray shaded areas in Fig. 1, bracketing the respective start and stop times. High-resolution X-ray grating spectra consist of photospheric continuum emission plus broad emission lines that varied greatly between the two observations (Ness et al. 2010), yielding a systematic increase in flux in lines of higher ionization stage.

2. X-RAY/UV OBSERVATIONS

Two 16-hour *XMM-Newton* observations were carried out with start times 2010 February 19.65 ($t_2 = t_0 + 22.9$ days) and 2010 March 3.7 ($t_3 = t_0 + 34.9$ days). Simultaneous X-ray light curves (0.1-1 keV), X-ray spectra (5-38 Å range, 0.01 Å resolution), and ultraviolet (UV) light curves and spectra (2200-3600 Å range, 15 Å resolution) were extracted from the European Photon Imaging Camera (EPIC), the Reflection Grating Spectrometer (RGS), and the Optical Monitor (OM), respectively. For day 22.9, 27 UV grism spectra (approximately 2000 seconds exposure time) were taken and were used to extract UV light curves by integrating over three different wavelength intervals: the full range, 2200-3600 Å, and the ranges 2800-3600 Å and 2200-2800 Å. In addition, we extracted an uncalibrated zero-order light curve from the non-dispersed photons which represent the brightness over a broad wavelength band with central wavelength ~ 4000 Å. Since the zero order is not flux calibrated, count rates are only presented as an indicator for relative brightness variations. For day 34.9, only band-integrated fluxes are available but in high time resolution of the OM fast mode.

Separate X-ray light curves were extracted in a soft (0.1-0.5 keV) and a hard (0.5-1 keV) band, S and H , and were used to compute a spectral hardness light curve $HR = (H - S)/(H + S)$.

3. LIGHT CURVES

TABLE 1
OBSERVATION LOG

ObsID 0650300201					ObsID 0561580301				
	Mode	Start Time (UT) MM-DD@HH:MM:SS	Exp (s)	counts s ⁻¹		Mode	Start Time (UT) MM-DD@HH:MM:SS	Exp (s)	counts s ⁻¹
MOS1	Large Window	Feb-19@15:41:19	63573	4.37 ^a	MOS1	Small Window	Mar-03@14:33:51	62557	5.47 ^a
MOS2	Timing Window	Feb-19@15:41:30	63308	4.28 ^a	MOS2	Small Window	Mar-03@14:33:51	62562	5.56 ^a
pn	Small Window	Feb-19@15:47:07	63365	25.90 ^a	pn	Small Window	Mar-03@14:39:24	62364	28.45 ^a
RGS1	Spectroscopy	Feb-19@15:40:20	63785	0.91 ^b	RGS1	Spectroscopy	Mar-03@16:52:22	54419	1.15 ^b
RGS2	Spectroscopy	Feb-19@15:40:25	63780	0.85 ^b	RGS2	Spectroscopy	Mar-03@14:32:42	62779	1.06 ^b
OM	UV grism	Feb-19@15:46:02	2000	11.1 ^c	OM	UVW1	Mar-03@14:38:19	2500	10.46 ^d 10.0 ^e
OM	UV grism	Feb-19@16:24:29	2000	11.7 ^c	OM	UVW1	Mar-03@15:25:06	2500	10.60 ^d 9.93 ^e
OM	UV grism	Feb-19@17:02:56	2000	11.6 ^c	OM	UVW1	Mar-03@16:11:53	2500	10.32 ^d 9.57 ^e
OM	UV grism	Feb-19@17:41:23	2000	10.0 ^c	OM	UVW1	Mar-03@16:58:40	2500	9.22 ^d 8.55 ^e
OM	UV grism	Feb-19@18:19:50	2000	8.81 ^c	OM	UVW1	Mar-03@17:45:27	2500	8.64 ^d 8.04 ^e
OM	UV grism	Feb-19@18:58:17	2000	7.27 ^c	OM	UVW1	Mar-03@18:32:14	2500	7.82 ^d 7.47 ^e
OM	UV grism	Feb-19@19:36:44	2000	5.64 ^c	OM	UVW1	Mar-03@19:19:01	2500	7.51 ^d 7.03 ^e
OM	UV grism	Feb-19@20:45:12	2000	6.28 ^c	OM	UVW1	Mar-03@20:05:48	2500	7.50 ^d 7.07 ^e
OM	UV grism	Feb-19@21:23:39	2000	8.77 ^c	OM	UVW1	Mar-03@20:52:35	2500	6.94 ^d 6.67 ^e
OM	UV grism	Feb-19@22:02:06	2000	9.75 ^c	OM	UVW1	Mar-03@21:39:22	2500	7.01 ^d 6.08 ^e
OM	UV grism	Feb-19@22:40:33	2000	10.9 ^c	OM	UVW1	Mar-03@22:26:09	2500	6.32 ^d 6.09 ^e
OM	UV grism	Feb-19@23:19:00	2000	12.3 ^c	OM	UVW1	Mar-03@23:12:56	2500	6.62 ^d 6.12 ^e
OM	UV grism	Feb-19@23:57:27	2000	12.3 ^c	OM	UVW1	Mar-03@23:59:43	2500	6.21 ^d 5.81 ^e
OM	UV grism	Feb-20@00:35:54	2000	12.5 ^c	OM	UVW1	Mar-04@00:46:30	2500	4.89 ^d 4.67 ^e
OM	UV grism	Feb-20@01:14:21	2000	12.4 ^c	OM	UVW1	Mar-04@01:33:17	2500	4.34 ^d 4.09 ^e
OM	UV grism	Feb-20@01:52:48	2000	13.3 ^c	OM	UVW1	Mar-04@02:20:04	2500	3.48 ^d 3.31 ^e
OM	UV grism	Feb-20@02:31:15	2000	15.1 ^c	OM	UVW1	Mar-04@03:06:51	2500	2.76 ^d 2.32 ^e
OM	UV grism	Feb-20@03:09:42	2000	12.5 ^c	OM	UVW1	Mar-04@03:53:38	2500	3.24 ^d 3.02 ^e
OM	UV grism	Feb-20@03:48:09	1980	12.1 ^c	OM	UVW1	Mar-04@04:40:25	2500	4.81 ^d 4.51 ^e
OM	UV grism	Feb-20@04:26:16	2000	13.3 ^c	OM	UVW1	Mar-04@05:27:12	3300	7.05 ^d 6.78 ^e
OM	UV grism	Feb-20@05:04:43	2000	13.4 ^c	OM	UVW1	Mar-04@06:27:19	3480	8.96 ^d 8.30 ^e
OM	UV grism	Feb-20@05:43:10	2000	13.4 ^c					
OM	UV grism	Feb-20@06:21:37	2000	13.0 ^c					
OM	UV grism	Feb-20@07:00:04	2000	12.2 ^c					
OM	UV grism	Feb-20@07:38:31	1940	13.3 ^c					
OM	UV grism	Feb-20@08:16:17	1800	13.0 ^c					
OM	UV grism	Feb-20@08:51:24	1700	12.8 ^c					

^aAverage of background subtracted light curve from *epic1ccorr*

^bAverage of background subtracted light curve from *rgslccorr*

^cIntegrated over dispersed grism spectra $\lambda = 2200 - 3600 \text{ \AA}$

^dFrom *omichain* using image data

^eAverage of background subtracted light curve from *omfchain* using fast window

In Fig. 2, a time series of X-ray brightness, X-ray hardness, UV flux, and zero-order (optical blue) count rate are shown as a function of orbital phase, based on Eq. 2. The optical and UV light curves (bottom two panels, error bars are smaller than the plot symbols) contain clean primary eclipses. The optical light curve is smoother than the UV light curve. The X-ray light curve (top panel) exhibits high-amplitude variations between two brightness levels (horizontal green and orange lines). The hardness ratio shown in the second panel is less variable than the X-ray brightness. A broad, flat peak may be seen that is centered around phase 1.0, indicating that softer emission from the central source may be eclipsed. The event at phase 1.21 could be a flare-like brightening, as anomalies are seen in all bands plus in the spectral hardness light curve; for more discussion on the spectral evolution, see Sect. 4.1.3. Possibly, also the sharp increase in X-rays plus reduction in spectral hardness at phase 0.9 could indicate a flare, but no simultaneous signatures in the UV/optical or hardness light curves support that. Note that similar sudden brightness increases have been seen in other novae, e.g., V1494 Aql

(Drake et al. 2003).

After phase 1.25 (quadrature), the count rate stabilized at the high-flux state for the remaining ~ 20 ks (≈ 5.5 hours), $\sim 30\%$ of the entire observation. This phenomenon is worth closer inspection because after phase 1.25, the X-ray dark secondary moves behind the X-ray bright photosphere which can then no longer be eclipsed. To investigate whether this could be a coincidence, we searched for other X-ray observations taken outside of eclipse, but found no similar occurrence in other data. The large majority of *Swift* observations (see Fig. 1) were centered around eclipses, and no continuous light curve outside eclipse can be assembled from these data that could confirm or reject this conclusion. It is noteworthy that Osborne et al. (2010) report typically lower flux around the time of eclipse, based on *Swift*/XRT data covering several eclipses. The *Chandra* light curve extracted from the observation on $t_1 = t_0 + 18.7$ days was taken outside eclipse, and no such variations were reported by Orio et al. (2010), but this observation was quite short (15 ks) and much earlier in the SSS phase. Although coincidence cannot be completely ruled out, we consider

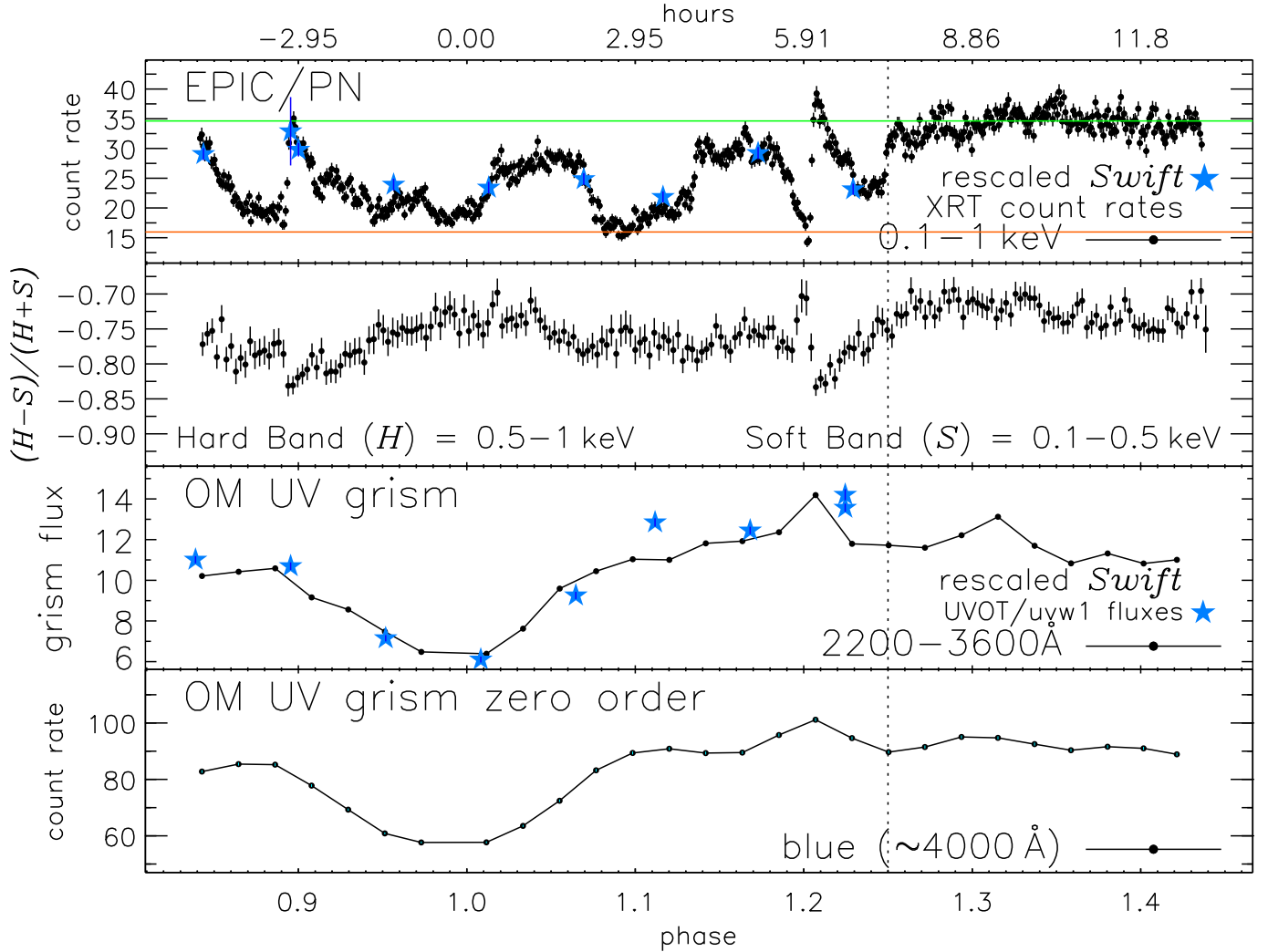


FIG. 2.— Short-term evolution of X-ray and UV/optical brightness and X-ray hardness (second panel) after $t_2 = t_0 + 22.9$ days, with bandpasses given in vertical axes and legends. Time units are phase, based on Eq. 2. Phase 1.0 is when the companion is between the white dwarf primary and the observer, and the vertical dotted line indicates quadrature phase. After phase 1.25, the companion is located behind the primary. In the top horizontal axis, hours relative to phase 1.0 are given. Simultaneous *Swift* data are added with blue star symbols, after scaling by a factor 25. UV grism fluxes are plotted in the third panel in units of $10^{-15} \text{ erg cm}^{-2} \text{ s}^{-1} \text{ Å}^{-1}$.

the fact that one third of the entire observation shows no dips as support for the conclusion that the variations are related to the binary orbit and therefore, that the occulted plasma resides inside the binary orbit.

Except for the two events at phases 0.9 and 1.21, we consider the patterns of variability as flux decrements (dips) with the undisturbed flux level being that observed after phase 1.25. An inhomogeneous brightness distribution that is eclipsed by the companion can securely be excluded, because during four minima the flux level drops to 50%. Each of four bright regions would have to contribute 50% to the total flux which is not possible.

The similar flux levels during minima and maxima leads us to the conclusion that the same source is occulted multiple times by different occulters. Since during the minima the flux is not zero, the central source can not contribute more than $\sim 50\%$ to the total X-ray emission, while the rest must originate from further away, e.g., caused by scattering in the outer regions of the ejecta (see also Sects. 4.1.1 and 4.1.3).

Within this picture, the totally different behavior in

the UV and optical can be explained by occulting plasma that is transparent to UV, only leaving visible a single eclipse by the companion. For example, neutral hydrogen is transparent to UV/optical light but opaque to soft X-rays. Alternatively, the X-ray emitting material that is likely more concentrated to around the white dwarf suffers sharper occultations by clumps while the larger optical emitting region will not have any significant fraction covered.

During the second *XMM-Newton* observation on day 34.9, the nova was already in the process of turning off, as is evident from a rapid decline in X-ray and UV brightness observed by *Swift* (Fig. 1 and Schaefer et al. 2010c). This can also be seen in the *XMM-Newton* light curves in Fig. 3, where the X-ray and UV light curves are shown in the top and bottom panels, respectively. *Swift*/XRT count rates, scaled by a factor 25 to compensate for different sensitivity, are also shown. The X-ray decline rate is marked by a dotted line with text above it. After conversion for different sensitivities, this rate is consistent with the long-term decline rate in the *Swift*/XRT light

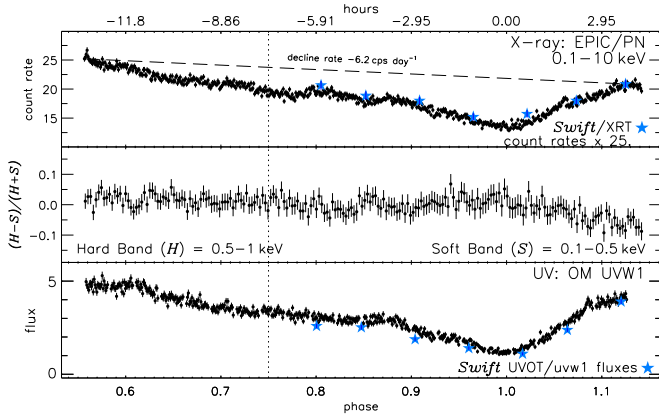


FIG. 3.— Evolution of X-ray and UV brightness (top and bottom) plus X-ray hardness (middle), taken on $t_3 = t_0 + 34.9$ days, as in Fig. 2. The dashed line in the top panel marks the X-ray decline rate of 6.2 cps day^{-1} and is consistent, after rescaling by the XRT-to-EPIC scaling factor of 25 (see caption of Fig. 2), with the long-term decline rate in the *Swift*/XRT data (see Fig. 1). In the bottom panel, UV fluxes from *XMM-Newton*/OM and *Swift*/UVOT are shown in units of $10^{-15} \text{ erg cm}^{-2} \text{ s}^{-1} \text{ \AA}^{-1}$. In both light curves, a small step is seen at phase ~ 0.6 and the light curves are asymmetric, yielding a sharper egress than ingress. This could indicate an occultation of the central source by an accretion stream that is located ahead of the path of the companion.

curve that is marked in Fig. 1.

The *Swift*/UVOT fluxes are consistent with the OM fluxes (bottom panel). A small step at phase ~ 0.62 can not be explained by an eclipse by the companion, but it could be an eclipse by an accretion stream (see §5).

A clean eclipse can be seen in all light curves centered around phase 1. The hardness light curve shown in the middle panel does not change with the eclipse. Towards the end of the observation, the source becomes slightly softer, possibly related to the decline.

The dips have disappeared from the X-ray light curve, and must therefore be understood as a transient phenomenon during the early SSS phase. This behavior appears similar to RS Oph and other novae that have been monitored with *Swift*, showing an early variability phase. The *XMM-Newton* data of U Sco give valuable insights into the processes that may explain such an early variability phase in more general terms.

3.1. Light curve model

As a qualitative test of the interpretation of occultations of the central source by dense absorbers, we have constructed a geometrical model which consists of two sources of light and four occulters. On a 350×350 brightness pixel map, two sources of light are defined, a non-variable, spherical central source with a radius R_{primary} plus additional constant emission that is not subject to occultations. Light originating from the central source is removed by the secondary star or by three clumps of gas that is optically thick to X-rays. All occulters are assumed to be spherical. In this way, a synthetic light curve can be generated by calculating for each phase bin the difference between the sources of light and the light originating from those pixels located behind the absorbers as seen from Earth.

The inclination angle and radii of the orbit and companion are well known and are fixed parameters. Unknown parameters are the sizes of the central source and the absorbers, the location of the absorbers, and their

opacity (see next paragraph). Values of these parameters were obtained by a combination of manual and automatic iteration with the aim to obtain good agreement between the synthetic and the observed light curves. Many different configurations are possible such as a non-spherical geometry of the source or the absorbers as well as intrinsic variability. Under these circumstances, we do not believe that beyond a qualitative feasibility test, reliable quantitative conclusions can be derived.

The opacity of the absorbers is parameterized by the column density of neutral atomic hydrogen, N_{H} . Depending on this value, a certain fraction of soft X-ray emission that originates from behind a given absorber can penetrate, yielding full transparency for $N_{\text{H}} = 0$. The fraction of light that can pass through the absorber, $T(w_i)$, depends on wavelength w_i : $T(w_i) = e^{-N_{\text{H}} \times \sigma(w_i)}$, where $\sigma(w_i)$ is the cross section for a given wavelength bin w_i and was computed using the *bamabs* tool which is part of the *PintofAle* package (Kashyap & Drake 2000). The fraction of absorbed light, integrated over the entire spectrum, $sp(w_i)$, is $F = 1 - \sum_i \{T(w_i) \times sp(w_i)\} / \sum_i sp(w_i)$.

In Fig. 4, a graphical illustration of a best-fit model to the X-ray light curve from day 22.9 is shown in the top. Below, the resulting light curve and the residuals relative to the observed X-ray light curve and the residuals relative to the measurement errors (χ) are shown. Except for the flare-like event at phase 1.2 and the sharp rise at phase 0.9, all residuals are consistent with the degree of variability after phase 1.25 and can be considered as not related to occultations. Further refinements of this model will not increase the precision of the conclusion.

While the degree of reproduction is not great, $\chi_{\text{red}}^2 = 4.7$, we attribute the deficiencies to additional random intrinsic variability that can not be parameterized. The parameters of this model are, for the central source, a radius of $R_{\text{primary}} = 0.67 R_{\odot}$ (17% of the Roche Lobe) and a brightness level of 16.6 counts per second. A power-law surface brightness distribution with a power law index α was assumed, but the index came out very small with $\alpha = -5.8 \times 10^{-5}$. We experimented with limb darkening or -brightening but found no better reproduction of the data. The level of additional constant emission was 17.7 counts per second. The nature of the additional non-variable emission is discussed in the context of the spectra in Sect. 4.1.1 and 4.1.3. The absorbers are assumed to orbit at a radius of $3.55 R_{\odot}$, having a size of 0.73, 1.1, and $0.83 R_{\odot}$, respectively. For the column density in the absorbers, a lower limit of $N_{\text{H}} > 1.4 \times 10^{21} \text{ cm}^{-2}$ is determined. This is illustrated in Fig. 5 from which it can be deduced that N_{H} is unconstrained at high values. We conclude that the absorbers are completely opaque to the X-ray spectrum of U Sco, and the lower limit represents the value above which only the constant additional emission remains. This can be compared to predictions from the expected density of the accretion disk material and the path length through it. The volume of a flared disk rim is of the order of 10^{34} cm^3 , e.g., Drake & Orlando (2010). For a mass loss rate of $\sim 10^{-7} M_{\odot} \text{ yr}^{-1}$ (e.g., Hachisu et al. 2000), and a build-up time of ~ 5 days, the accretion disk rim density is of order $3 \times 10^{14} \text{ cm}^{-3}$. For a path length through the gas of $\sim 0.1 R_{\odot}$, the column density is of order 10^{24} cm^{-2} . While this is higher than

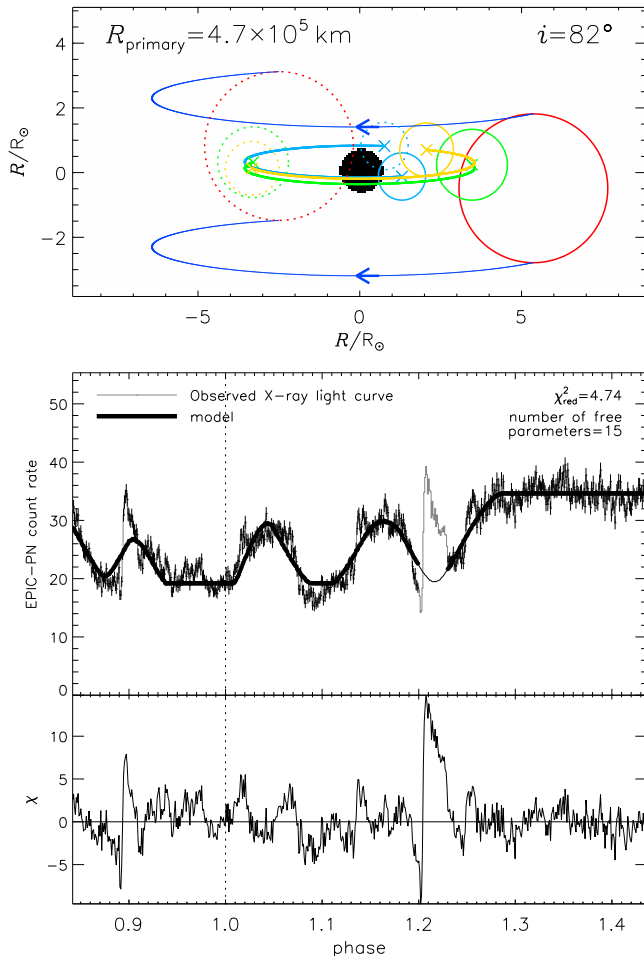


FIG. 4.— Qualitative geometrical model to the X-ray light curve taken on day 22.9. The top panel gives a spatial representation of the model as seen from Earth (inclination angle given in top right legend) and is to scale with units given in the axis labels. The location and size of the central source is marked by the black filled circle, centered at the origin of the coordinate system and the assumed radius given in the top left legend. The central source is eclipsed by the companion (red circle) and by three co-rotating absorbers (blue, green, and orange circles). The sizes and positions of the circles are to scale with the solid and dotted styles denoting the respective positions at the start and the end of the observation. Eclipses by any of these occulters lead to temporary decreases in total light that, in the absence of eclipses, is assumed to be constant. Additional emission is added that remains constant, regardless of binary phase. The resulting model light curve is shown in comparison to the data in the middle panel. The bottom panel shows the difference between data and model, relative to the measurement errors, $\chi = (\text{data} - \text{model})/\Delta$. Except for two events at phases 0.9 and 1.2, the residuals between model and data are of the same order as the variations outside eclipse, past phase 1.25.

the number derived from the eclipse model, a fraction of all hydrogen can be ionized, requiring a higher column density for the same opacity, or the build-up time may be shorter. Moreover, the disk may not have fully reformed at the time of observation, and during the reformation process, the density should be lower.

The vertical dotted line in the bottom two panels of Fig. 4 indicates phase 1.0, where the center of eclipse by the companion should be. A dip of the expected width is present, however, it is clearly shifted. For better reproduction of the data, we had to include a phase shift parameter with a value of -0.026 in the model. Such an

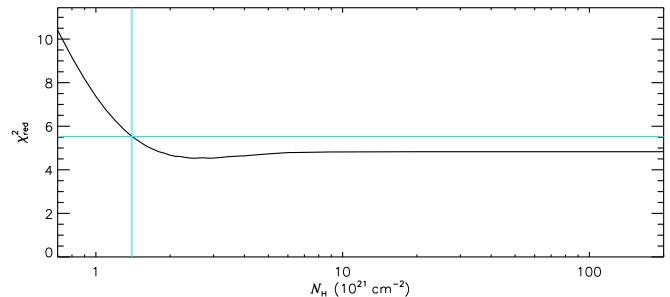


FIG. 5.— Determination of column density of absorbers in light curve model. While the light model yields poor resemblance with observations for low values of N_H , any high value of N_H is consistent with the data.

artificial shift could be avoided if a non spherical symmetry of the central X-ray source is allowed. For example, we tested a model with a crescent shaped source and were able to reproduce the second dip without a phase shift. There is, however, no physical explanation for a crescent shaped central source.

The same procedure was applied to the 27 OM grism exposures of day 22.9. We constructed two separate UV light curves by integrating each grism spectrum over the two wavelength bands 2200-2800 Å and 2800-3600 Å. Combined with the light curve from the non-dispersed photons, we have three light curves representing different spectral colors, all containing clear eclipses. In Fig. 6, the results are illustrated, where the red circles represent the location and relative size of the companion during each of the 27 exposures and the shaded circles in the center represent the primary with the best-fit radii for each band, following the color scheme given in the top right legend. The best-fit radii are given in the top left legend. The short-wavelength UV band yields the smallest radius, while the longest-wavelength optical band (zero order) yields the largest radius, close to the inner Lagrangian point. The significance of the light curve fit is illustrated in Fig. 7, where a range of primary radii is plotted against changes in χ^2 relative to the best fit for each wavelength band. The boundaries around the 1- σ uncertainties are marked by the vertical colored lines, based on an increase of χ^2 by 1 (horizontal black line). The best-fit light curve models are shown in comparison to the data (in normalized units) in the bottom panel of Fig. 6. While the models (points connected by lines, see bottom right legend) give no perfect reproduction of the data (shaded areas and gray line, see top left legend), the width of the respective eclipses are well reproduced, yielding reliable radius estimates.

The trend of decreasing radius with decreasing wavelength appears like a temperature gradient. Hotter plasma, producing more short-wavelength emission, resides closer to the center than cooler plasma.

4. SPECTRA

The X-ray spectra from two types of spectrometers are discussed in §4.1. High-resolution soft grating spectra and low-resolution hard CCD spectra are available for both observations. In addition, 27 UV grism spectra have been taken during the first observations that are discussed in §4.2.

4.1. The X-ray spectra

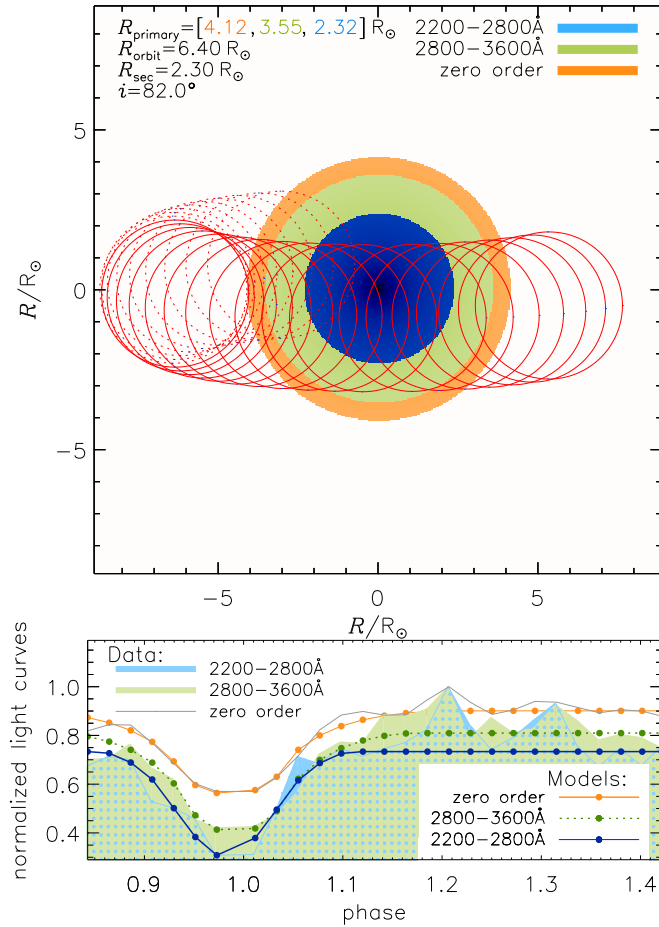


FIG. 6.— Geometrical light curve model applied to three UV/optical light curves extracted from the non-dispersed zero grism order (optical, orange) and two UV light curves (green and blue), extracted from different wavelength ranges as denoted in the upper right legend. The central source was assumed spherical with a power-law brightness distribution and the resulting best-fit radii for each wavelength band given in the top left legend. The three emitting regions are illustrated as filled circles. The location and size of the companion is plotted as a red circle at the beginning of each of the 27 exposures. In the **bottom panel**, the three observed light curves (shades) and the best-fit models (points) are shown in normalized units.

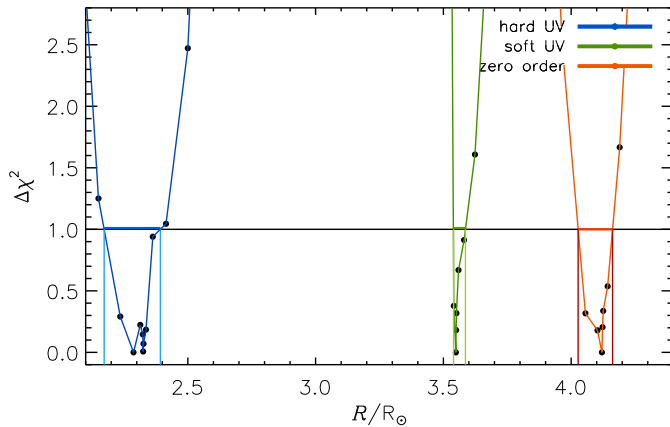


FIG. 7.— Estimate of uncertainties in the primary radius obtained from three UV/optical light curves, using the color scheme defined in Fig. 6 (see legend).

XMM-Newton carries two types of X-ray spectrometers that give information from different energy bands, yielding different sensitivity and spectral resolution. The EPIC consists of two types of CCD detectors, the MOS (Metal Oxide Semi-conductor; Turner et al. 2001) and the pn (Strüder et al. 2001). Two identical MOS cameras, MOS1 and MOS2, are in operation behind two separate mirrors, and they can be operated in different modes. They are sensitive between 0.1–10 keV with an effective area ranging between 50–500 cm² and an energy resolution of roughly 50 eV. The pn has a lower resolution of 100 eV but a higher sensitivity of 200–1300 cm² from 0.1–10 keV because of the larger collecting area of an extra set of mirrors.

The dispersive spectrometers RGS1 and RGS2 (den Herder et al. 2001) share the light with the same mirrors as the MOS cameras. They are both sensitive between 6–38 Å (0.3–2 keV) with an effective area between 20–60 cm² and a wavelength resolution of 0.05 Å. The dispersed photons are recorded by MOS type CCDs. The intrinsic energy resolution of the detectors is used to separate higher dispersion orders from the first dispersion order spectrum. While the sensitivity of the RGS is much lower than the EPIC, the superior resolving power of $\Delta E/E \sim 100–600$ compared to $\Delta E/E < 1$ for EPIC allows individual line transitions to be identified. For example, only in the RGS spectrum can an absorption line spectrum be distinguished from an emission line spectrum, provided the source is bright enough or the exposure time is sufficiently long for enough signal to noise. SSS spectra are extremely bright and are therefore ideally suited for studies with the RGS. The EPIC spectra are superior above ~ 2 keV and are used to study the hard Wien tail and to search for harder emission that may be related to shocks in the surrounding medium, or accretion.

Separate spectra for different time intervals can be extracted by application of filters on photon arrival times. We have extracted the RGS and EPIC spectra from the entire observations and a series of spectra from adjacent shorter time intervals in order to probe for spectral time evolution. Times were converted to orbital phase using Eq. 2.

4.1.1. High-resolution RGS spectra

The merged RGS1+RGS2 spectra from both observations are shown in photon flux units in Fig. 8. The spectra shown here have been produced with the SAS command `rgsfluxer`. The spectral range of the RGS covers the peak of the absorbed photospheric emission from the optically thick ejecta. A combination of continuum emission and strong emission lines can be identified.

As a parameterization of the continuum component, we fitted a blackbody model to those spectral bins that are not dominated by strong emission lines. The resulting models are marked by the yellow/blue curves in Fig. 8 for each observation (see caption). The resulting parameters effective temperature, interstellar neutral hydrogen column density, and effective radius (derived from dilution factor and assumed distance 12 kpc) are given in the left legends. The bolometric luminosity, derived from these values applying the Stefan-Boltzmann law, are also given but an unrealistically high value is derived

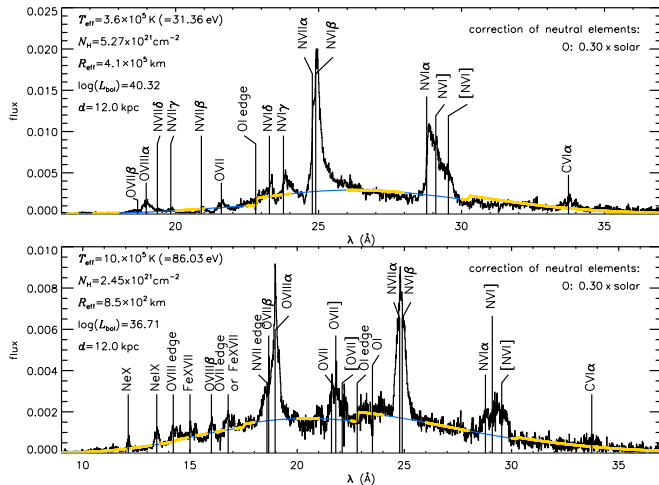


FIG. 8.— RGS spectra taken on day 22.9 (top) and 34.9 (bottom). Flux units are $\text{ph cm}^{-2} \text{s}^{-1} \text{\AA}^{-1}$. A blackbody curve is included as blue/yellow line, where those spectral bins that were used for fitting are yellow. The best-fit parameter values are given in the left legends but the main purpose of the blackbody fitting is to show that the continuum component is of atmospheric origin. The photospheric temperature has greatly increased from day 22.9 to day 34.9, evidenced by a clear shift of the Wien tail to shorter wavelengths. Additional strong emission lines are marked with labels. Lines of higher ionization stages are seen on day 34.9, yielding additional evidence for a temperature increase.

for day 22.9, exceeding the Eddington luminosity by two orders of magnitude. This is a well-known deficiency of blackbody fitting to SSS spectra (e.g., Krautter et al. 1996), and we therefore caution that these values can not be trusted to reflect the true physical conditions, and they are only given for reproducibility. Appropriate models have to account for radiation transport in non-local thermal equilibrium (NLTE), plus the expansion of the ejecta has to be taken into account (e.g., Ness 2010; van Rossum & Ness 2010). These are currently unsolved problems, and their discussion is beyond the scope of this paper. Nevertheless, the reproduction of the continuum component by a blackbody model is sufficiently good to allow the conclusion that the continuum originates from the photosphere around the white dwarf. The absence of any absorption lines could indicate that we are not directly seeing the atmospheric emission. Gray scattering in a plasma of fast electrons (Thompson scattering) could explain this observation, as narrow atmospheric features would be smeared out.

While the photospheric temperature can not be accurately determined from blackbody fits, the location of the Wien tail clearly indicates that the temperature must be well above 10^5 K. From this lower limit of the temperature we can conclude that the radial extent must be significantly smaller than the radius of the Roche Lobe ($4.1 R_{\odot}$). Otherwise, the bolometric luminosity would be four orders of magnitude above the Eddington limit which is physically unrealistic.

The emission lines originate from highly ionized nitrogen, oxygen and carbon. For N VII and N VI, the H-like and He-like $1s$ - np series can be identified up to δ ($1s$ - $5p$). In the second observation, additional Ne IX and Ne X lines can be identified.

In order to escape, the emission lines must originate in a reasonably optically thin plasma, which can reside at

any distance, far above the photosphere. On the other hand, the strongest lines are seen at wavelengths where the continuum is strongest, and they are thus likely photoexcited, requiring that they come from hot plasma residing close to the ionizing source.

This type of X-ray spectrum, in both observations, is not typical of novae such as V4743 Sgr, RS Oph, or V2491 Cyg in which prominent deep photospheric absorption lines were seen by Ness et al. (2003, 2007, 2011). It resembles more that of the eclipsing supersoft source Cal 87 which Ebisawa et al. (2010) explain as a combination of Thompson scattered continuum plus emission lines from resonant line scattering as viewed at high inclination angle (see also Greiner et al. 2004). The photosphere around the white dwarf cannot be seen directly as it is blocked by the accretion disk. A similar situation may be occurring in U Sco and perhaps even in all high-inclination systems as was already suggestive from UV observations presented by La Dous (1991) and Vitello & Shlosman (1993). Thompson scattering in the electron-rich environment would preserve the spectral color, but a non-zero velocity distribution of electrons would smear out photospheric absorption lines which can explain the absence of any clear indication of absorption lines in the RGS spectra of U Sco.

In addition to Thompson scattering, resonant line scattering may occur, selectively amplifying or diminishing resonance emission lines, depending on the geometry of the scattering plasma. For example, the geometry of an accretion disk allows more photons from resonance transitions to be scattered into the line of sight than out of the line of sight, and resonance lines can appear amplified when compared to forbidden lines. This is best seen in the He-like N VI triplet at 28-29 Å, where the resonance line is stronger than the intercombination line. For comparison, in the high-resolution X-ray spectra of low-density stellar coronal plasma, the forbidden line is usually almost equally as strong as the resonance line and stronger than the intercombination line (Ness et al. 2001). While the low ratio of forbidden to intercombination can be interpreted as high densities (Gabriel & Jordan 1969), the same low ratio can also be caused by strong UV radiation fields, if the emitting plasma resides close to the photosphere. Inspection of dip and non-dip spectra presented in Sect. 4.1.3 confirms this explanation.

4.1.2. *EPIC spectra*

EPIC spectra yield the best information about the high-energy part of the spectrum, above 2 keV, where the RGS is not sensitive. *Swift* detected hard emission early in the evolution (Schlegel et al. 2010a), and it is of interest to use the deeper *XMM-Newton* EPIC data to check whether it was still present on days 22.9 and 34.9.

In Fig. 9, the photon image of MOS1 taken on day 22.9 is shown with all events in the left panel and only those with registered energies above 2 keV in the right panel. While in the right panel, a clear source seems to be present, this can not be interpreted as the detection of hard emission. The blue circle marks the radius within which significant pile up is present, which was determined using the SAS tool `epatplot`. All photons in the right panel are within this circle, indicating that they are contaminated by pile up. We encountered the same problem

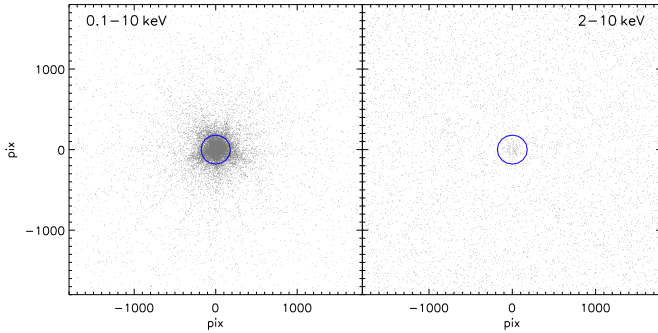


FIG. 9.— EPIC/MOS1 observation taken on day 22.9. In the left panel, the pixel positions of all events between 0.1-10 keV are shown relative to the peak of the point spread function. In the right panel, only photons between 2 and 10 keV are shown. A concentration of counts towards the source position can be seen, however, the inner 180 pixels (marked by the blue circle around the center) are affected by pile up (see text).

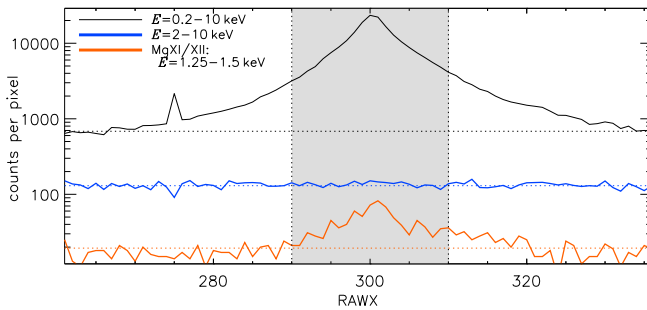


FIG. 10.— EPIC/MOS2 timing mode observation taken on day 22.9. In this mode, all photons along the detector y axis (RAWY) are accumulated into a single number of counts for each detector x-pixel (=RAWX) coordinate. The source spectrum was extracted from between RAWX values 290-310 (marked by gray shaded area), encircling 74% of all counts. Plotted is the number of counts per pixel, integrated over three different energy ranges as indicated in the legend. Above 2 keV, no significant detection is found. The energy range 1.25-1.5 keV contains the H-like and He-like Mg lines.

in the pn observation and in all EPIC observations of the second observation.

More sensitive to faint hard emission are the MOS2 data in the first observation which was operated in timing mode (see Table 1), yielding a shorter readout time. We determined, with `epatplot`, that pile up was not a problem. In Fig. 10, the brightness profiles as a function of the detector coordinates (RAWX) are shown for three different energy ranges as indicated in the legend. The full-range profile clearly indicates the location of the source in RAWX coordinates, and above 2 keV, nothing is seen at the same position. In the narrow range 1.25-1.5 keV, containing the H-like and He-like Mg lines, a clear detection is found, indicating that some harder emission above the SSS component is present. A source spectrum can be extracted from a range in RAWX of 290-310 pixels, which is marked by the gray shaded area in Fig. 10. No other sources are located along the y axis that could contaminate the source region. For our further considerations, we therefore only use the MOS2 spectrum for the first observation while for the second observation, we use the most sensitive pn data, after correction for pile up.

The EPIC spectra for days 22.9 and 34.9 are shown in Fig. 11. The energies of some line transitions that have been seen in other novae are marked with vertical lines

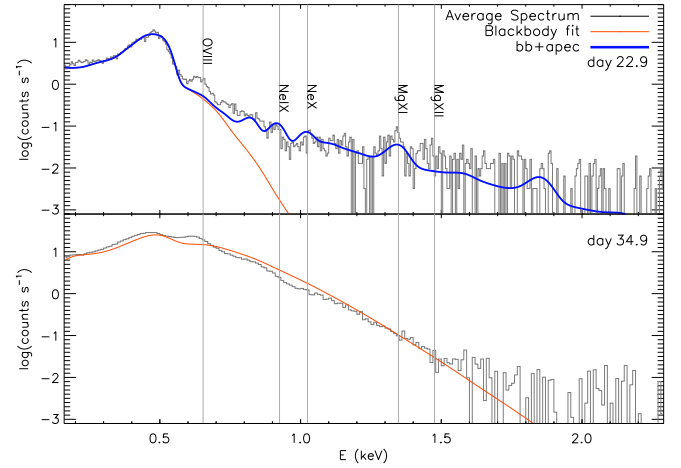


FIG. 11.— EPIC spectra taken on days 22.9 (top, MOS2 detector) and 34.9 (bottom, pn detector). The energies of strong H-like and He-like transitions are marked, and the red lines indicate blackbody models with the same parameters as used in Fig. 8. For day 22.9, a model with an additional optically thin collisional component (APEC) is plotted with a blue thick line.

with labels.

The SSS continuum appears featureless at EPIC energy resolution. Blackbody models with the same parameters as used in Fig. 8 are overplotted with the red curves. Obviously, the EPIC spectra are not suitable for studies of the soft part below 2 keV, even if they are not piled up. However, in the first observation, there is significant excess emission above the blackbody curve at energies $\gtrsim 0.7$ keV, indicating the presence of an additional plasma component. This excess can be modeled with an optically thin thermal APEC model (Smith et al. 2001) as indicated by the blue thick curve in Fig. 11. The APEC model component assumes collisional equilibrium for ionization and excitation processes which is observable as bremsstrahlung continuum plus emission lines. Optically thin emission has been seen in various novae before, see, e.g., Lloyd et al. (1992); Krautter et al. (1996); Mukai & Ishida (2001); Orío et al. (2001), and can be caused by shocks with pre-existing surrounding material, e.g., from previous outbursts, or within inhomogeneous ejecta. The electron temperature obtained from fitting an APEC model plus a blackbody component with fixed parameters to the spectrum is $kT = 0.29 \pm 0.03$ keV. This temperature corresponds to an average random electron velocity of 10^9 cm s $^{-1}$ when assuming a Maxwellian velocity distribution, which is approximately twice the expansion velocity. The H-like and He-like Ne and Mg 1s-2p lines are well reproduced by the APEC model component. The O VIII line at ~ 0.66 keV (18.97 Å) is not reproduced by the combined bb+apec model and is more likely photoionized by the SSS continuum. In the second observation the collisional component has faded significantly.

Above 2 keV, we found no significant continuum emission nor Fe fluorescent lines and lines of Fe XXV at 6.4 and 6.7 keV, respectively. A more detailed discussion of the evolution of the hard emission will be instructive in the context of all X-ray observations, including the early *Swift* and *Suzaku* data.

4.1.3. Spectral Evolution

A) Long term evolution

A comparison of the spectra from the two observations yields the spectral evolution on time scales of days to weeks. A trend of increasing temperature has been reported by Ness et al. (2010) based on increasing strengths in high ionization lines from day 18.7 to day 22.9. A gradual increase of the effective temperature is expected as the photospheric radius continues to shrink during the SSS phase. From the spectra shown in Figs. 8 and 11, this trend can be seen to have continued through day 34.9, evidenced by a clear shift of the Wien tail of the continuum to higher shorter wavelength and the stronger emission lines belonging to high-ionization stages (Fig. 8). Only the high-ionization He/H-like Mg lines are stronger on day 22.9 than on day 34.9 (Fig. 13). Since they are not formed on top of any continuum emission, they can not be photoexcited. The more likely origin of the Mg and Ne lines is a collisional plasma, and this interpretation is supported by the APEC model.

B) Short term evolution

To study the short term evolution, we have extracted multiple RGS and EPIC spectra covering adjacent time intervals. In Figs. 12 and 13, the spectra and pn light curves, rotated by 90 degrees, are shown in the top and right panels, respectively. The central parts are brightness maps with increasing orbital phase from top to bottom and increasing wavelength/energy from left to right for the RGS and EPIC data, respectively. The key to the color scheme is given in the top right. In addition, the hardness light curves shown in the second panels of Figs. 2 and 3 are used for the discussion.

To illustrate the effects of contamination of the high-energy part of the EPIC spectra by solar flare activity, field-integrated flare particle background light curves are shown with light blue color in Fig. 13. To determine the particle background, a full-field light curve was extracted above 10 keV. For better comparison, the particle background light curve is amplified by a factor 20. Above 2 keV, no significant emission can be identified in the EPIC spectra of either observation. Around phase 1.3 in the first observation and phase 0.85 in the second, some harder emission was present that could be contamination because it coincides with elevated levels of solar flare particle background emission.

We have also extracted separate RGS spectra for times during dips and peaks for day 22.9 and in- and outside of eclipse for day 34.9. A combined dip spectrum has been extracted from the time intervals (in spacecraft units 10^8 s after 1998-01-01) 3.8298385 – 3.8298715, 3.8298925 – 3.8299995, and 3.8300645 – 3.8301275. A peak spectrum is integrated over the five time intervals 3.8298166 – 3.8298362, 3.8298726 – 3.8298878, 3.8300018 – 3.8300620, 3.8301286 – 3.8301858, and 3.8302500 – 3.8304502. The inside eclipse spectrum was extracted from the time interval 3.8404789 – 3.8407309 and the outside eclipse spectrum from 3.8401449 – 3.8403669. During extraction, the spectra were binned to 0.1-Å bins, larger than the default 0.01 Å for better signal to noise. The differences between the resulting spectra are shown in Fig. 14. The shaded areas around the difference spectra

represent the uncertainty ranges derived via error propagation from the measurement errors in the individual spectra. If the times of low flux are interpreted as occultations of emission originating from within the binary orbit, the difference spectra are representative of the plasma residing in the inner orbit while the low-flux spectra represent only outer regions.

B1) Flare-like events

Two significant brightness increases occurred around phases 0.9 and 1.2 in the first observation which in the following are referred to as flares. In the top panel of Fig. 12, it can be seen in the contour levels that both events were accompanied by increased emission in the N VI lines which originate from lower ionization plasma than the other emission lines. During the flare at phase 1.2, some extra emission in the N VI intercombination line can be seen. At the same time, the N VII Ly α line at 24.8 Å continues to be fainter during the dip while the higher Ly series lines of N VII seem to peak around the same time as the N VI lines.

The contemporaneous appearance of the lower-temperature line with both flare-like events is unexpected because flares are usually high-temperature events involving some heating mechanism. For example, in solar and stellar coronae, flare events are usually accompanied by the appearance of high-ionization emission lines which are produced directly in the flare (e.g., Güdel et al. 2004).

When assuming photospheric events as origin of the flares and that the N VI line emission has responded to these changes, then a time delay of ~ 0.01 in phase, corresponding to ~ 17 minutes after the peak of each flare, can be used to derive the maximum distance between the plasma that emits the excess in N VI and the photosphere. The two black horizontal dashed lines in Fig. 12 illustrate the time delay, and it corresponds to a light travel distance of ~ 2 AU. This is outside of the binary orbit of $6.5 R_{\odot}$ where cooler plasma resides. Hotter plasma further inside may have been blocked during the times of the flares, as both occurred during dips.

B2) Spectral changes on day 22.9 (dipping)

Closer inspection of the spectral changes with the dips in the first observation gives insights into the geometry of the emitting gas at this time. The brightness map in the top panel of Fig. 12 illustrates that during the dips, the continuum and the emission lines are both fainter, but neither component is completely occulted. Both components must therefore originate from both, the inner orbit and from further outside. Thompson scattering of the continuum component has already been discussed in Sect. 4.1.1 to resolve the conflict between high temperature from the Wien tail and the required small size of the central source plus the absence of absorption lines.

A comparison of the emission lines during and outside dips on day 22.9 can be studied in Fig. 14. The difference spectrum represents the plasma within the inner orbit, revealing the spectral signatures of resonance line scattering. While the strong 1s-2p resonance lines of, e.g., N VII (24.78 Å) and N VI (28.74 Å) originate only from the outer regions, lines belonging to transitions involv-

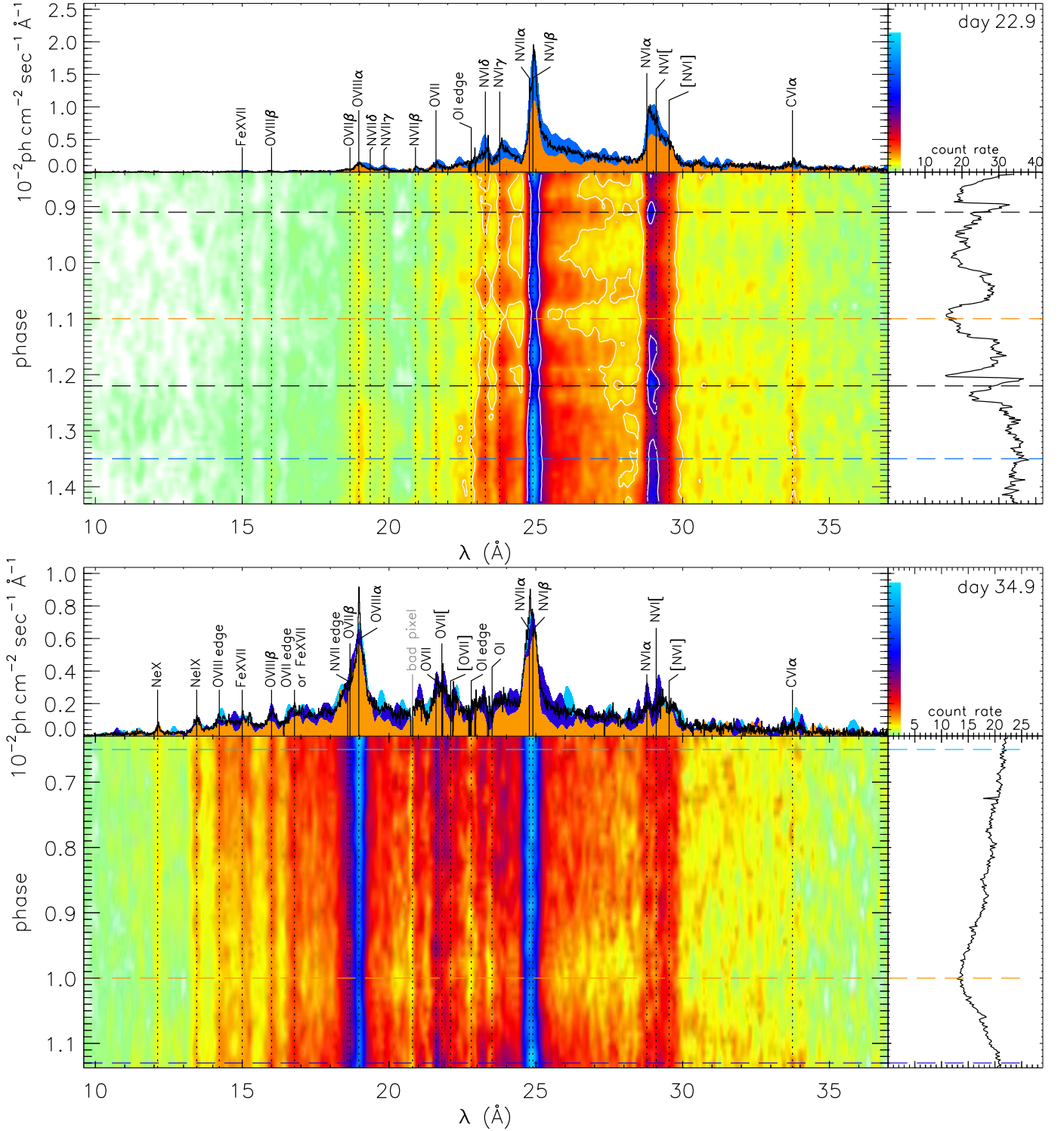


FIG. 12.— Illustration of time evolution of RGS spectra taken on days 22.9 (top) and 34.9 (bottom). The central part in each plot is a brightness map composed of 63 and 54 separate spectra (1000 s exposure time), respectively, with colors representing increasing flux levels from light green, yellow, red, purple, dark blue, and light blue. The corresponding flux for each color can be determined using the vertical legend bar in the top right. In the top panel, two isocontour levels are included in white. Increasing wavelengths are plotted from left to right, and increasing phase from top to bottom; phases have been calculated from photon arrival times based on Eq. 2. The dashed horizontal lines running across the brightness map indicate selected times for which the corresponding spectra are shown with colored shades in the top panel. In addition, the average spectra from Fig. 8 are included. In the right, the pn light curves from the top panels of Figs. 2 and 3 are shown, rotated by 90° clockwise. The dips in the top panel and the eclipse in the bottom panel are seen in both continuum and emission lines in the brightness map. Flare-like events at phases 1.21 and 0.9 on day 22.9 yield an increase in the N VI lines at $\sim 29 \text{ \AA}$. The two black lines illustrate a time lag between flares and the changes in N VI that correspond to a light travel distance of 2 AU.

ing higher principal quantum numbers are stronger in the difference spectrum, e.g., the N VI He-like series lines

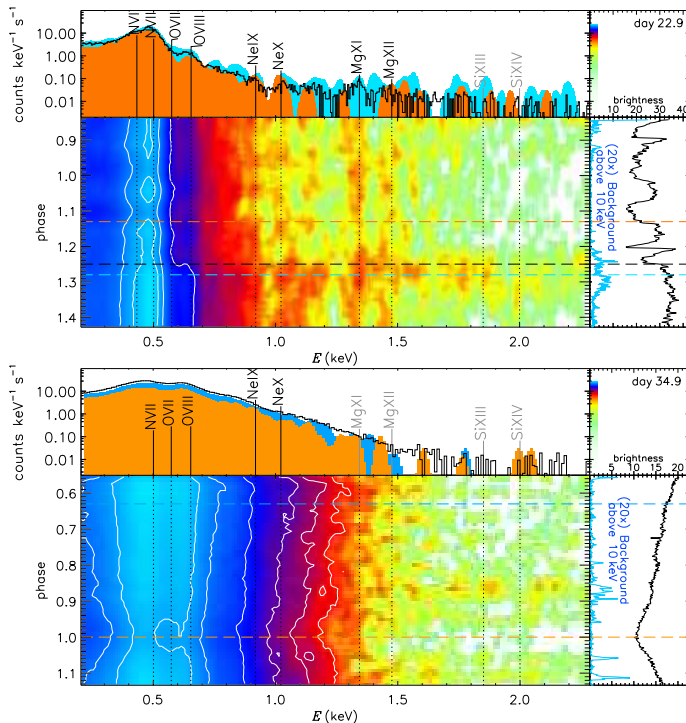


FIG. 13.— Illustration of the spectral evolution in the 0.2-2.7 keV band in the same format as explained in the legend to Fig. 12, based on 63 and 62 EPIC spectra, extracted from adjacent time intervals in the observations, starting day 22.9 (top, MOS2 detector) and 34.9 (bottom, pn detector), respectively. The white lines in the brightness maps are isocontours. The energies of strong H-like and He-like transitions are marked in the top parts (see also Fig. 11). In the right, the same pn light curve from the top panel of Fig. 2 is shown, rotated by 90° clockwise. In addition, the field-integrated light curves extracted from above 10 keV are shown to illustrate times at which solar flare activity may compromise the high-energy part of the spectra.

He β , γ , and δ . The respective oscillator strengths are $f = 0.17$, 0.05, and 0.02, which are low compared to the oscillator strength of the He α line of $f = 0.71$. Line photons with high values of f can be absorbed and re-emitted in a different direction. In a non-spherical plasma, strong resonance lines can be amplified or reduced, compared to lines of lower oscillator strengths. The fact that we are seeing the high- f lines from the inner regions reduced is consistent with the geometry of an accretion disk.

Forbidden transitions can not be absorbed, and the contributions from the inner region to the ratio of the NVI intercombination and forbidden lines at 29.1 and 29.54 Å is unaltered by resonance scattering. Owing to the proximity to the central source, the low f/i ratio reported in Sect. 4.1.1 has to be interpreted as photoexcitation rather than high density.

In the top panel of Fig. 13, the evolution of the Wien tail can be studied that is a qualitative indicator for the photospheric temperature. During dips, the continuum emission has gone down at all wavelength, and no shift of the Wien tail can be seen that would indicate that the continuum component from the outside regions has a different temperature. This supports the interpretation of Thompson scattering. The sudden change in the variability pattern at phase 1.25 is accompanied by a sudden increase in brightness above 0.6 keV, extending to ~ 1.5 keV, including the MgXI 1s-2p transition at 1.3 keV. While solar flare activity could be held respon-

sible for the brighter emission between phases 1.2-1.35, the spectra taken after phase 1.35 are not contaminated and are still harder. This could be interpreted in the general context of increasing temperature on longer time scales as discussed above. Also, a slight increase in the high-ionization OVIII line is suggestive in the top panel of Fig. 12, but it may also be part of the general increase in brightness.

B3) Spectral changes on day 34.9 (eclipse)

The spectral evolution during the second observation is displayed in the bottom panels of Figs. 12 and 13. The continuum and the emission line components experience similar changes during the eclipse as during the dips on day 22.9. The total emission decreases by $\sim 50\%$ during eclipse, indicative of significant scattering processes. The emission lines decrease by roughly the same amount as the continuum.

This is illustrated with the difference spectra shown with blue color in Fig. 14. The NVI and NVII lines are hardly present, and therefore, *all* the plasma emitting the observed N lines resides outside of the binary orbit while some of the flux in the hotter OVIII line also originates from within the orbit. In order to explain the changes from day 22.9 to 34.9, the line emission that was first seen to come from the inner regions (NVI He β and intercombination line) has to be moved to further outside to escape eclipses by the companion on day 34.9. While for the NVI He-like intercombination line one could argue that the entire NVI triplet is too faint for studies of changes, the line complex around 25 Å is strong enough that residual NVI He β would be detectable. Also, the higher Ly series lines of NVII are not seen in the difference spectrum. We interpret the absence also of high Ly series lines in the difference spectrum as evidence for an increase in the optical depth of the scattering plasma, which could be part of the reformation process of the accretion disk. A bit puzzling appears the presence of OVIII Ly α in the difference spectrum while Ly β is not present.

Except for the OVIII Ly α line, the reduction in brightness during eclipse can therefore exclusively be attributed to the continuum. The shape of the continuum in the difference spectrum in Fig. 14 is the shape of the continuum component in the inner regions. It has roughly the same shape as the out-of-eclipse spectrum, supporting the interpretation of achromatic Thompson scattering.

Close inspection of the RGS and EPIC brightness maps in the bottom panels of Figs. 12 and 13 reveals that the eclipse progresses in a slightly non-uniform way in wavelength/energy. In the Rayleigh-Jeans tail, between 26-28 Å, the continuum seems to go through a wider eclipse towards longer wavelength (Fig. 12). In the Wien tail, the eclipse seems to be narrower towards higher energies which is indicated by the contours in Fig. 13. This could indicate a temperature gradient, however, the hardness light curve in the middle panel of Fig. 3 does not indicate a significant temperature change with the eclipse. Only the softening after the eclipse appears noteworthy and may have to be attributed to the cooling while nuclear burning is turning off. On the other hand, the hardness light curve contains the emission lines and is a less

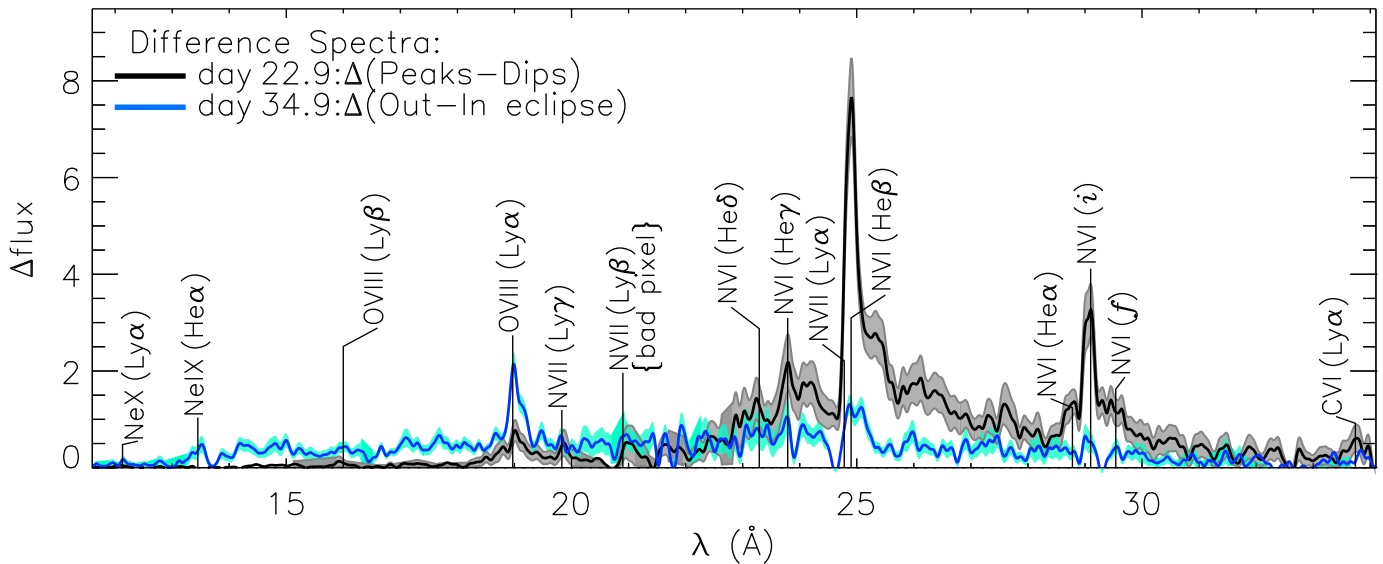


FIG. 14.— Difference spectra between dip- and peak spectra for day 22.9 (gray) and in- and out of eclipse spectra for day 34.9 (light blue), representing the spectra of the missing emission during dip and eclipse, respectively, thus from the inner-binary region. The indices Ly α , β , and γ indicate H-like Lyman series lines with 1s-2p to 1s-4p transitions, and He α to δ are the respective He-like series lines with transitions 1s-2p to 1s-5p. The notation He α , i , and f behind the N vi labels indicate He-like 1s-2p transitions with 1S - 1P (resonance line), 1S - 3P (intercombination line), and 1S - 3S (forbidden line), respectively. The N vi intercombination line (i at 29.1 Å) and the He-like series lines β to δ originate from the inner orbit on day 22.9 and are thus photoexcited by the nearby photospheric continuum emission. The N vi He α line is reduced in the inner-orbit spectrum because of resonant line scattering out of the line of sight. The O viii resonance line at 18.97 Å on day 34.9 reaches us more directly from the inner regions while the N lines are reduced by the same amount as the surrounding continuum.

sensitive indicator for the photospheric temperature.

4.2. UV spectra

In the first of the two *XMM-Newton* observations, starting day 22.9, the UV grism of the OM was employed, taking 27 consecutive spectra (see Table 1). In Fig. 15, these spectra are shown in the same format as in Figs. 12 and 13. In the range 2200-3600 Å, the spectrum shows many features which are difficult to identify. Wavelengths of a few known lines are marked. A weak feature coincides with the position of the 2800 Å Mg II resonance doublet but, given the presence of many similar features in the spectrum as well as the uncertainty of the absolute wavelength scale (which depends on the accurate centroiding of the zero order), its identification is uncertain.

The wavelength range of the OM grisms overlaps with the long-wavelength range of the International Ultraviolet Explorer (IUE). Five spectra were taken with the IUE during the outburst in 1979: on June 28, June 30, July 2, July 4, and July 10, corresponding to 5, 7, 8, 10, and 16 days after outburst (Williams et al. 1981). In the top panel of Fig. 15, the IUE spectra from 8 and 16 days after the 1979 outburst are overplotted in orange and blue (see right legend). The strongest lines in these spectra are, apart from the Mg II doublet, He II at 2512, 2734 and 3204 Å, Ne IV at 2421 Å and [Mg V] at 2784 and 2928 Å.

The eclipse minimum can be seen to coincide with reductions in flux at all wavelengths in the brightness image, but some spectral ranges, e.g., ~ 2350 Å, yield narrower eclipses than others, e.g., ~ 3200 Å. The two dashed black lines in the image draw attention to the possibility of broader eclipses towards longer wavelengths as found in §3.1 for the two wavelength bands 2200-2800 Å

and 2800-3600 Å. If these bands are interpreted as spectral colors, the conclusion would be that hotter plasma resides further inside. However, the concept of spectral color as temperature indicator is only valid for continuum sources while emission lines can arise at any wavelength, independently of their formation temperature. While emission lines of higher ionization stages are produced closer to the central ionizing source, they do not necessarily arise at shorter wavelengths. It can be seen that some features, e.g., at 2650 Å, have indeed narrower eclipse profiles than others, e.g., at 3125 Å. Also, not all features have their eclipse minimum at the same phase, suggesting that, if they are real lines, they arise from different emission regions in an inhomogeneous plasma.

5. DISCUSSION

The different behavior in the simultaneous *XMM-Newton* X-ray and UV light curves starting on day 22.9 was unexpected with a clear eclipse only in UV and optical but multiple dips in the X-rays. Some similarities with the class of X-ray dippers (Walter et al. 1981, 1982) may be helpful in discussing possible scenarios. For example, Díaz Trigo et al. (2009) presented in their figure 5 the *XMM-Newton* X-ray and UV light curves of the high-inclination X-ray binary XB 1254-690 and found clear eclipses in the V band while in the X-ray band, deep dips were seen at phase 0.8. While multiple dips are generally not seen in the X-ray dippers, EXO 0748-676 contained dips at phases 0.6, 0.7, 0.8, 0.9 and 0.1 (see figure 9 in Parmar et al. 1986). While a number of similarities are thus seen, U Sco is still a completely different system, and any parallels to X-ray dippers have to be interpreted with care.

In X-ray dippers, significant changes in spectral X-ray hardness have oftentimes been observed, while

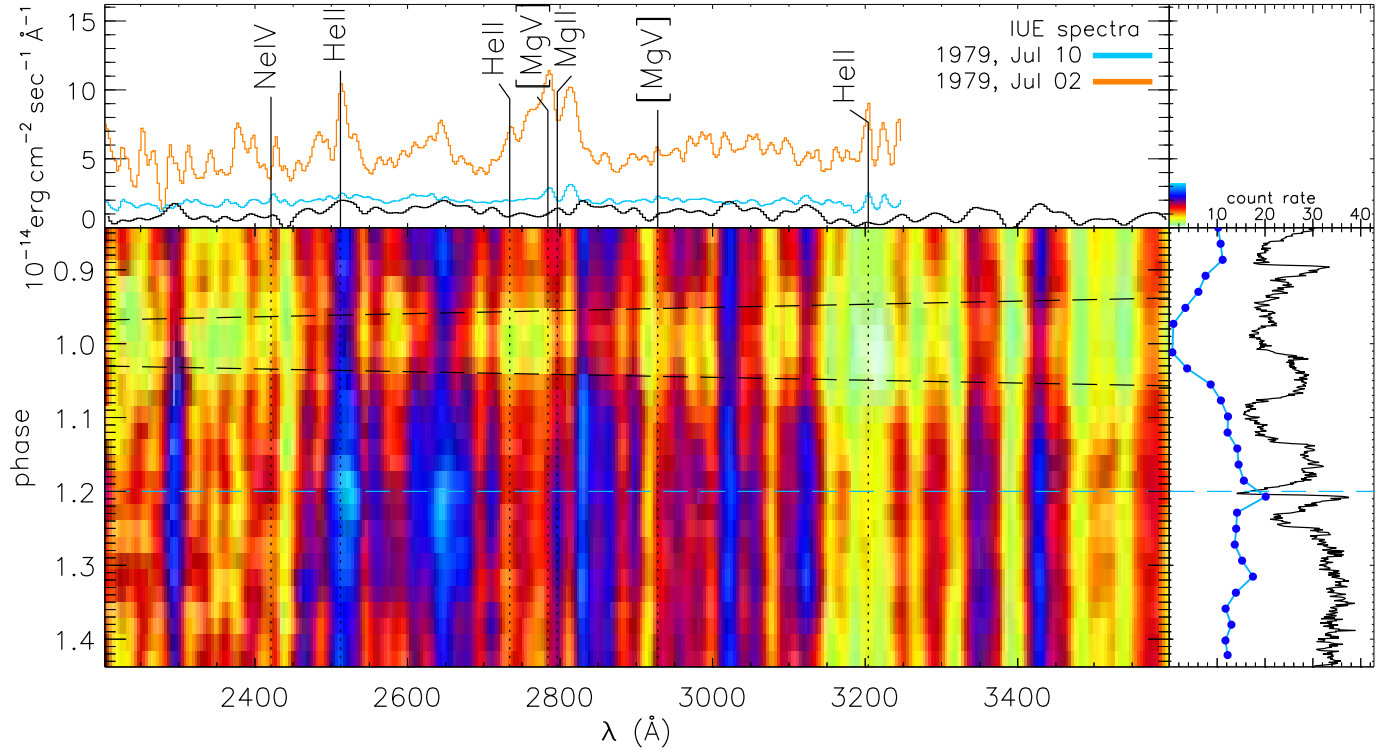


FIG. 15.— Illustration of the spectral evolution in the same format as Fig. 12 for 27 OM U grism observations, starting on day 22.9. In the top panel, two IUE spectra taken 8 and 16 days after the 1979 outburst of U Sco are included in orange and blue as indicated in the right legend. In the right panel, the X-ray light curve and the OM light curve are shown in black and blue, respectively. The two diverging black dashed lines in the central panel are drawn to guide the eye, indicating a possible trend of broader eclipse towards longer wavelengths. The light blue dashed line indicates the time of the flare at phase 1.2.

in U Sco, the hardness remained the same during dips. An achromatic steep decrease in flux has also been seen by Sala et al. (2008) in the nova V5116 Sgr. In contrast to U Sco and other novae, the central object in X-ray dips is an accreting neutron star, emitting a much harder continuum. Harder X-rays can partially penetrate material of large column densities, and only the soft tail of the X-ray spectrum is blocked. The continuum spectrum of U Sco is much softer, and any material of significant column density above $\sim 10^{21} \text{ cm}^{-2}$ will block all emission from behind, regardless of energy. Total disappearance of all X-ray light during dips is only avoided because of Thompson scattering of the central emission into a much larger region rather than partial transparency of the absorbers. Our parameter studies of N_H in the light curve model support this interpretation (see Fig. 5). An example of achromatic dipping at low energies as a consequence of high- N_H absorbers in relation to the shape of the source spectrum is Cyg X-2 (Bałucińska-Church et al. 2011). While the continuum is much harder than in U Sco, the opacity of the absorbers is $\sim 10^{23} \text{ cm}^{-2}$, leading to full blockage of all light in the 0.5-2 keV band. The hardness ratio from 0.5-1.0/1.0-2.0 band is therefore constant during the dips, while only emission from the 4.5-8.0 keV band can partially penetrate. In U Sco, not enough emission at energies above 1 keV is present to constrain N_H of the absorbers in the way this is possible for Cyg X-2.

A question of interest is the reformation of the accretion disk that was destroyed during the nova outburst (Drake & Orlando 2010). The transition from

dipping on day 22.9 to clean eclipse on day 34.9 may be part of the reformation process, and the concept of intersecting opaque clumps as part of the reformation process deserves closer consideration. The theoretical possibility of clumps in the ejecta has been discussed by Diaz et al. (2010), however, being immersed in a high-radiation environment, the ejecta must be highly ionized, and as such, they do not absorb soft X-rays via the photoelectric effect. Thompson scattering in clumpy material can also be ruled out as cause for the dips as that would also lead to the same dips in the UV/optical light curves. Clumpy ejecta can therefore not cause such deep dips in the X-ray light curve. A possible source of opaque clumps consisting of cooler material is the companion star, if accretion has set in again. Cooler plasma is opaque to soft X-ray while at the same time being transparent to light with wavelengths longer than 912 Å (13.6 eV), the ionization energy of atomic hydrogen, which would explain why no dips are seen in the simultaneous UV and optical light curves. Absorbing atomic material from the companion is thus strong support for the interpretation that accretion has set in again. This does not require the full reestablishment of the accretion disk, a clumpy accretion stream can also be imagined. The absence of dips after phase 1.25 suggests that no clumpy material is on the far side as seen from the companion which is an argument in favor of an accretion stream, residing between the companion and the central white dwarf.

In Fig. 16, we show a theoretically calculated initial trajectory of a reforming disk based on equations 1 and

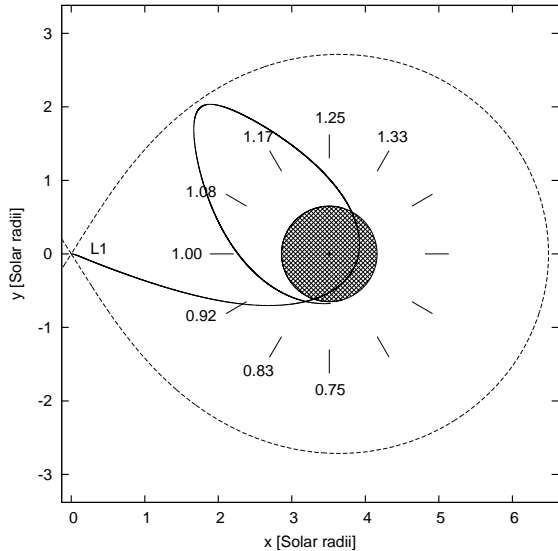


FIG. 16.— Trajectory of accretion stream at an early time of the reformation of the accretion disk. The calculation follows Flannery (1975) using the parameters of U Sco. The trajectory interacts with itself, forming an asymmetric ring at the beginning of disk reformation. The radius of the central source is drawn assuming the radius derived from the light curve model (see top panel of Fig. 4), which is also consistent with the blackbody radius. The trajectory dives into the optically thick ejecta on the far side from the inner Lagrangian point (L1). This could explain the residual variability seen in the bottom panel of Fig. 4. Being inside the photosphere, this part of the accretion stream does not occult the photospheric X-ray emission. No dips are therefore expected between phases 1.33 and 0.75, while during other times, dips can occur, depending on the structure of the accretion stream. At a later time, the circular ring that is the protodisk interacts with the incoming stream, leading to circularization that could lead to the disappearance of dips in X-rays as seen on day 34.9 (see Fig.3).

2 in Flannery (1975), assuming the parameters of U Sco. During the early disk formation phase, an asymmetrical “ring” is formed. The phases that correspond to different viewing angles are marked. The hashed area in the center encircles the optically thick parts of the ejecta. The surface can be considered the source of X-ray emission, and no views inside are possible. The highly elliptical trajectory runs through the optically thick part of the ejecta, and any inhomogeneities inside the photosphere can not cause dips. An eccentric trajectory of infalling material can thus be the explanation for not seeing any dips after phase 1.25.

A remarkably similar event has been observed by in’t Zand et al. (2011) in the accreting neutron star in 2S 0918-549. After an X-ray burst, strong ($87 \pm 1\%$ peak-to-peak amplitude) achromatic fluctuations were seen as a transient phenomenon. Since the outburst evolved much more rapidly, the X-ray light curve taken with the Proportional Counter Array (PCA) on the Rossi X-ray Timing Explorer (RXTE) may be interpreted as a fast-motion picture of the evolution in U Sco (see figure 1 in in’t Zand et al. 2011). It was speculated by in’t Zand et al. (2011) that the fluctuations were due to Thompson scattering by inhomogeneities in a resettling accretion disk that was disrupted by the effects of super-Eddington fluxes, much like in U Sco where the blast wave has destroyed the accretion disk (Drake & Orlando 2010). Furthermore, they argue that an expanding

shell may be the necessary prerequisite for the fluctuations. Irregularities in the accretion stream could be caused by the continued expansion of the nova ejecta that has stopped between days 22.9 and 34.9. The stream could be disrupted by the ejecta, or the companion star may be distorted in the outer layers. A difference to in’t Zand et al. (2011) is the interpretation of the properties of the intervening material, yielding highly ionized plasma. Dips are caused by Thompson scattering out of the line of sight rather than photoelectric absorption. This is consistent with their observation of increases above the decay trend of the burst which can be explained by sideways or backward scattering of clouds located behind the compact object. Such increases are not seen in U Sco. Furthermore, achromatic Thompson scattering would also leave its footprints in the UV and optical light curves, and photoelectric absorption by high- N_H plasma in a low state of ionization appears more likely for U Sco.

6. SUMMARY AND CONCLUSIONS

From the simultaneous *XMM-Newton* X-ray, UV, and optical observations of the 10th recorded outburst of the recurrent, eclipsing nova U Sco, we have deduced new insights into time variability, spectral properties, and spatial structure:

- **Time variability:** As opposed to expectations that eclipse mapping will reveal the photospheric radius of the white dwarf in different stages of the evolution, we have seen achromatic dipping in X-rays but clean eclipses in UV and optical. Dips were only seen before quadrature, phase 1.25. The later observation contains clean eclipses in all bands. During dips and eclipses, $\sim 50\%$ of X-ray emission remained, indicating that the observed X-ray emission is extended beyond the binary orbit.
- **Spectral Properties:** The high-resolution X-ray spectra consist of blackbody-like continuum emission plus strong emission lines. No absorption lines can be identified. From day 22.9 to day 34.9, an increase in temperature can be deduced from the shape of the continuum and from increases in emission lines arising in ions of higher ionization stages. The eclipsing supersoft source Cal87 yields a qualitatively similar high-resolution X-ray spectrum. Photospheric X-ray emission from the central source is blocked by the accretion disk and can only be seen after Thompson scattering in the accretion disk corona. Strong emission lines come from resonant line scattering within the surrounding optically thin medium. Only emission lines from transitions with low oscillator strengths are seen to originate directly from the inner regions. The UV grism spectra on day 22.9 contain emission lines that undergo eclipses, which indicates that they originate from within the inner binary orbit. The interpretation as an emission line spectrum is supported by a comparison to the 1979 outburst, during which the UV spectra were already optically thin 7 days after outburst.
- **Evolution of the Spatial Structure:** We interpret the dipping as the result of occultations of the

central source by high-density absorbing gas that is aligned along the trajectory of a reforming accretion stream. The gas consists of plasma of low ionization stage, originating from the companion star. The continued outflow disrupts the accretion stream into fragments that intersect the line of sight. After nuclear burning has ceased, the outflow stops, no more fragmentation takes place, allowing the accretion stream to circularize and condense into a flat accretion disk, yielding no more dips.

One important argument in favor of reestablishment of accretion is the low degree of ionization of the intervening material which indicates that it originates from the companion. The most important supporting observations are the achromatic nature of dips and the lack of dips in the other wavelength bands. Ionized plasma would not cause any photoelectric absorption while low-ionization plasma is only opaque to soft X-rays but transparent to optical/UV emission, longward of 912 Å. While the dips could be caused by Thompson scattering in the electron-rich environment of the highly ionized nova ejecta, the same dips would have to be seen in UV and optical.

The observed spectral signatures for combined Thompson scattering and resonant line scattering are:

- The continuum component does not go to zero during either dips or eclipse. The location of the Wien tail requires the source to be small enough for complete occultations to avoid super Eddington luminosity. Achromatic Thompson scattering can increase the geometric size of the emission region without changing the shape of the continuum. Photospheric absorption lines are smeared out in the fast-moving scattering plasma and are there-

fore not resolved.

- Our diagnostics of dip and non-dip spectra revealed that only emission lines from transitions with low oscillator strength originate directly from the inner regions. During dips, the flux in strong resonance lines is lower by the same amount as the surrounding continuum, indicating that they are scattered out of the line of sight, leaving us to only see them after resonant scattering.

The observed history of the reformation of the accretion disk in U Sco is likely applicable to formation of accretion disks in general, although the time scales may depend on system parameters, which bears closer investigation via theoretical simulations.

Based on observations obtained with *XMM-Newton*, an ESA science mission with instruments and contributions directly funded by ESA Member States and NASA. We'd like to thank the *XMM-Newton* Science Operations Centre for efficient scheduling and generously granting Director's Discretionary Time for the second observation. B.E.S. was supported under a grant from the National Science Foundation (AST 0708079). AD was supported in part by the Grand-in-Aid for the global COE programs on "The Next Generation of Physics, spun from Diversity and Emergence" from MEXT and also by the Slovak Grant Agency, grant VEGA-1/0520/10. KLP acknowledges support from STFC. JJD was supported by NASA contract NAS8-39073 to the *Chandra X-ray Center*. SS acknowledges support from NASA+NSF grants to ASU. MH acknowledges support from MICINN project AYA 2008-01839/ESP, AGAUR project 2009 SGR 315 and FEDER funds and GS MICINN projects AYA 2008-04211-C02-01 and AYA 2007-66256. GS acknowledges MICINN grants AYA2008-04211-C02-01 and AYA2010-15685, and ESF EUROCORES Program EuroGENESIS grant EUI2009-04167.

REFERENCES

- Balućńska-Church, M., Schulz, N. S., Wilms, J., Gibiec, A., Hanke, M., Spencer, R. E., Rushton, A., & Church, M. J. 2011, *A&A*, 530, A102
- den Herder, J. W., et al. 2001, *A&A*, 365, L7
- Díaz, M. P., Williams, R. E., Luna, G. J., Moraes, M., & Takeda, L. 2010, *AJ*, 140, 1860
- Díaz Trigo, M., Parmar, A. N., Boirin, L., Motch, C., Talavera, A., & Balman, S. 2009, *A&A*, 493, 145
- Drake, J. J., & Orlando, S. 2010, *ApJL*, 720, 195
- Drake, J. J., et al. 2003, *ApJ*, 584, 448
- Ebisawa, K., Rauch, T., & Takei, D. 2010, *AN*, 331, 152
- Flannery, B. P. 1975, *MNRAS*, 170, 325
- Gabriel, A. H., & Jordan, C. 1969, *MNRAS*, 145, 241
- Greiner, J., Iyudin, A., Jimenez-Garate, M., Burwitz, V., Schwarz, R., DiStefano, R., & Schulz, N. 2004, in *Revista Mexicana de Astronomia y Astrofisica Conference Series*, Vol. 20, *Revista Mexicana de Astronomia y Astrofisica Conference Series*, ed. G. Tovmassian & E. Sion, 18
- Güdel, M., Audard, M., Reale, F., Skinner, S. L., & Linsky, J. L. 2004, *A&A*, 416, 713
- Hachisu, I., Kato, M., Kato, T., & Matsumoto, K. 2000, *ApJL*, 528, L97
- in't Zand, J. J. M., Galloway, D. K., & Ballantyne, D. R. 2011, *A&A*, 525, 111
- Kahabka, P., & van den Heuvel, E. P. J. 1997, *ARA&A*, 35, 69
- Kashyap, V., & Drake, J. J. 2000, *Bulletin of the Astronomical Society of India*, 28, 475
- Krautter, J., Ögelman, H., Starrfield, S., Wichmann, R., & Pfeffermann, E. 1996, *ApJ*, 456, 788
- La Dous, C. 1991, *A&A*, 252, 100
- Lloyd, H. M., O'Brien, T. J., Bode, M. F., Predehl, P., Schmitt, J. H. M. M., Truemper, J., Watson, M. G., & Pounds, K. A. 1992, *Nature*, 356, 222
- Mason, E. 2011, *ArXiv e-prints*
- Mukai, K., & Ishida, M. 2001, *ApJ*, 551, 1024
- Ness, J. 2010, *Astronomische Nachrichten*, 331, 179
- Ness, J., et al. 2010, *The Astronomer's Telegram*, 2469, 1
- Ness, J.-U., et al. 2001, *A&A*, 367, 282
- . 2003, *ApJL*, 594, L127
- . 2007, *ApJ*, 665, 1334
- . 2011, *ApJ*, 733, 70
- Orio, M., Nelson, T., Luna, J., Schaefer, B., Page, K., Beardmore, A., & Osborne, J. 2010, *The Astronomer's Telegram*, 2451, 1
- Orio, M., et al. 2001, *MNRAS*, 326, L13
- Osborne, J. P., et al. 2010, *The Astronomer's Telegram*, 2442, 1
- Parmar, A. N., White, N. E., Giommi, P., & Gottwald, M. 1986, *ApJ*, 308, 199
- Robinson, E. L. 1976, *ARAA*, 14, 119
- Sala, G., Hernanz, M., Ferri, C., & Greiner, J. 2008, *ApJL*, 675, L93
- Schaefer, B. E. 1990, *ApJL*, 355, L39
- . 2010, *ApJS*, 187, 275
- Schaefer, B. E., Harris, B. G., Dvorak, S., Templeton, M., & Linnolt, M. 2010a, *IAUC*, 9111, 1

- Schaefer, B. E., et al. 2010b, *AJ*, 140, 925
—, 2010c, *The Astronomer's Telegram*, 2477, 1
Schlegel, E. M., et al. 2010a, *The Astronomer's Telegram*, 2419, 1
—, 2010b, *The Astronomer's Telegram*, 2430, 1
Smith, R. K., Brickhouse, N. S., Liedahl, D. A., & Raymond, J. C. 2001, *ApJ*, 556, L91
Starrfield, S., Sparks, W. M., & Shaviv, G. 1988, *ApJL*, 325, L35
Strüder, L., et al. 2001, *A&A*, 365, L18
Thoroughgood, T. D., Dhillon, V. S., Littlefair, S. P., Marsh, T. R., & Smith, D. A. 2001, *MNRAS*, 327, 1323
Turner, M. J. L., et al. 2001, *A&A*, 365, L27
van den Heuvel, E. P. J., Bhattacharya, D., Nomoto, K., & Rappaport, S. A. 1992, *A&A*, 262, 97
van Rossum, D., & Ness, J.-U. 2010, *AN*, 331, 175
Verbunt, F. 1982, *SSRv*, 32, 379
Vitello, P., & Shlosman, I. 1993, *ApJ*, 410, 815
Walter, F. M., Mason, K. O., Clarke, J. T., Halpern, J., Grindlay, J. E., Bowyer, S., & Henry, J. P. 1982, *ApJL*, 253, L67
Walter, F. M., White, N. E., & Swank, J. 1981, *IAUC*, 3611, 2
Williams, R. E., Sparks, W. M., Gallagher, J. S., Ney, E. P., Starrfield, S. G., & Truran, J. W. 1981, *ApJ*, 251, 221